A combined approach of Atom Probe Tomography and unsupervised machine learning to understand phase transformation in $(Al_xGa_{1-x})_2O_3$

Jith Sarker[1], Scott Broderick[1], A F M Anhar Uddin Bhuiyan[2], Zixuan Feng[2], Hongping Zhao[2,3], and Baishakhi Mazumder[1]*

[1]*Department of Materials Design and Innovation, University at Buffalo, Buffalo, NY 14260, USA*
[2]*Depertment of Electrical and Computer Engineering, The Ohio State University, Columbus, OH 43210, USA*
[3]*Department of Materials Science and Engineering, The Ohio State University, Columbus, OH 43210, USA*
*Corresponding author: *baishakh@buffalo.edu*

Abstract: In this paper, we investigated the evolution of microstructural chemistry of metal organic chemical vapor deposition grown (010) $(Al_xGa_{1-x})_2O_3$ films with varying Al content, x = 0.10-1.0 using atom probe tomography (APT). At low Al content ($x \leq 0.25$), the films are homogeneous, where layer inhomogeneity appears at high Al content ($x > 0.25$). Further increasing the Al content up to $x \geq 0.60$ results in a homogeneous $(Al_xGa_{1-x})_2O_3$ layer. This change in microstructural features were linked to phase transformation of $(Al_xGa_{1-x})_2O_3$ using a manifold learning approach to capture the governing features hidden in the data dimensionality. Combining APT to unsupervised machine learning enables APT to be an independent material characterization tool to investigate microstructure, chemical composition and phase related information.

β-Ga_2O_3 based ultra-wide bandgap semiconductors have drawn extensive attention recently due to their tunable bandgap ranging from 4.9 eV (β-Ga_2O_3) to 8.8 eV (α-Al_2O_3)[1], leading to a predicted high breakdown field of ~8 MV/cm and higher Baliga figure of merit (BFoM) compared to both *4H-SiC* and *GaN*[2,3]. These qualities make β-Ga_2O_3 based alloys highly promising for high power transistors and deep ultra-violet (DUV) photodetectors[4-7]. The bandgap of β-Ga_2O_3 is modified by tuning the alloy composition to realize design flexibility and heterostructure device optimization[8]. Prior efforts have reported the successful growth of $(Al_xGa_{1-x})_2O_3$ using various methods like molecular beam epitaxy (MBE)[9,10] and metal organic chemical vapor deposition (MOCVD)[11,12]. In these efforts, the aim was to grow phase stable $(Al_xGa_{1-x})_2O_3$ crystalline films with high Al content in order to design high bandgap devices with improved efficiency. Since β-Ga_2O_3 crystal is monoclinic while Al_2O_3 is corundum crystal structure system[9], there exists a solubility limit of Al_2O_3 in Ga_2O_3[13,14]. Increasing the Al content beyond this range results in appearance of unidentified chemical phases in $(Al_xGa_{1-x})_2O_3$ films[15]. Due to this solubility limit, β-phase stability was not achieved above Al content, x ~20% in MBE[16], and rather undetermined polycrystalline structure was obtained[9,16]. An emergence of corundum α-phase alongside monoclinic-β was reported for $(Al_xGa_{1-x})_2O_3$ grown by solution combustion synthesis at x~80%[1]. For MOCVD grown $(Al_xGa_{1-x})_2O_3$ films, a transition from single β to a mixed (β+γ)-phase was observed at x >27%[17]. The emergent γ-phase has a defective spinel cubic crystal structure and is thermally metastable unlike single monoclinic β-phase stable $(Al_xGa_{1-x})_2O_3$. These different phases lead to a degraded crystallinity in (β+γ)-$(Al_xGa_{1-x})_2O_3$ films due to inhomogeneous Al distribution[17]. Appearance of a single γ-phase was reported at x>0.78 for pulsed laser deposition (PLD)[18] grown films. In MOCVD grown $(Al_xGa_{1-x})_2O_3$, the reported Al contents till which single β-phase is retained varies over a range of ~27%[12] to ~40%[19]. Such discrepancies demand atomic level chemical investigation to determine the actual solubility limit of Al in $(Al_xGa_{1-x})_2O_3$ and to understand the related phase transformations.

Atom probe tomography (APT) is a powerful nanoscale analysis tool that provides elemental information of materials with the unique advantage of three-dimensional (3D) visualization of constituent elements, which is not possible with any other conventional characterization techniques[20]. APT is capable of the most accurate determination of atomic level chemical composition with sub-nanometer resolution and part-per-million (PPM) sensitivity[21]. This technique also provides the lateral chemical information from the growth surface that directly links to its chemical phase. While the technique relies on the removal of atoms and capturing individual ion positions in 3D that facilitates quantification of elemental distribution in complex structures, due to the huge amount of ions collected in APT some materials' features such as phase transitions remain hidden within the massive experimental data[22-24]. A data mining strategy is integrated here to extract the patterns in APT data by capturing the "latent" phase related information, which influences the variation of structural chemistry of the materials and the corresponding properties. Principal component analysis (PCA) reduces the dimensionality of a dataset while retaining most of the information[23]

and by transforming multi-component tensorial quantities of directionally correlated variable sets into a linearly uncorrelated variable set referred to as principal components (PCs)[23]. By minimizing the data dimensionality, PCA provides principal alignment directions based on how much variance in the data is captured. Interpretation of the variance of material features captured by these PCs can capture the deviations in the corresponding properties (phase transitions for instance[24]) due to change in materials microstructure and chemistry. The use of PCA here allows us to assess the relationships between chemistry and microstructure/phase formation by converting the complex data into an interpretable format.

In this letter, we systematically investigated the evolution of microstructure and chemistry of MOCVD grown $(Al_xGa_{1-x})_2O_3$ films with varying Al content from low ($x = 0.10$) to high ($x = 1.0$) to assess the crystal quality using APT. PCA was performed as a complementary data mining approach to link structural chemistry to phase transitions occurring in $(Al_xGa_{1-x})_2O_3$, thus enabling APT as a complete material characterization tool without requiring any other supplemental characterization techniques. Information here reported would be significant for not only the $(Al_xGa_{1-x})_2O_3$ film growth condition optimizations but also would offer insights about material properties and underlying physics for design and fabrication of high performance β-$(Al_xGa_{1-x})_2O_3$ devices.

In our recent work, we studied the phase transformation of MOCVD grown $(Al_xGa_{1-x})_2O_3$ on (010) Ga_2O_3 substrates as the Al content varies from 0-100% using complementary characterization techniques including scanning transmission electron microscopy (STEM), X-ray diffraction (XRD) and APT[17]. The study revealed that, at relatively low Al content ($x < 0.3$), $(Al_xGa_{1-x})_2O_3$ is single monoclinic β-phase while it transforms to γ-phase at high Al content ($x > 0.5$) with a mixed (β+γ) phase in between. The present work is an in-depth study in which we introduced advanced data mining on APT data to capture the phase transformations occurring in $(Al_xGa_{1-x})_2O_3$ as Al content varies. Two different $(Al_xGa_{1-x})_2O_3$ thin films with $x = 0.10$-0.30 and $x = 0.10$-1.0 were grown on Fe-doped semi-insulating (010) β-Ga_2O_3 substrates, the details of the sample structures are reported elsewhere[12,17]. APT samples were prepared using focused ion beam (FIB) milling method[25]. The APT data acquisition was conducted using a UV laser pulse with pulse energy of 20 pJ, detection rates of 0.005% and base specimen temperature of 50 K. The CAMECA Integrated Visualization and Analysis Software (IVAS 3.8.5a34) was employed for the tip reconstruction. The 3D atom maps of the probed regions were generated via tip profile reconstruction using a high magnification SEM tip image. Tip profile reconstruction yields the best result when multilayers are present[26]. PCA was performed on the time-of-flight (TOF; the time between application of the laser pulse and the evaporated atom hits the detector[26]) of ions obtained from APT for both samples to extract phase related information. The single APT TOF spectrum was sampled into multiple TOF spectra to create a high dimensional data set (with rows representing different equally sampled regions and columns representing the counts at a given TOF within the region), which was input into the PCA analysis done through MATLAB. PCA provides principal alignment directions by minimizing the dimensionality of the sampled TOF spectra. Principal component 1 (PC1) represents the direction of the highest variation in the data. Principal component 2 (PC2) being orthogonal to PC1, represents the variable that is the second highest in terms of variance[23]. From the PC1 vs. PC2, information of phase transformation was extracted in both cases. Of note, since we are analyzing spectral input, the analysis is deconstructing the initial input data to the most prominent patterns in the TOF spectra along with the corresponding weightings on those spectral patterns, thereby maximizing the information captured by assessing only the most dominant signals. The procedure illustrating the preprocessing of the raw TOF data and PCA analysis is described by the flowchart shown in supplementary Fig. S4.

Figure 1(a) depicts the 3D atomic distribution of the $(Al_xGa_{1-x})_2O_3/Ga_2O_3$ heterostructure where the $(Al_xGa_{1-x})_2O_3$ film possesses a layered structure with different Al compositions of $x = 0.10$, 0.15, 0.20, 0.25 and 0.30, along the growth direction. Al atoms are represented by red spheres while blue spheres correspond to Ga atoms. The schematic of this heterostructure is depicted in supplementary Fig. S1(a). To investigate the alloy chemistry with varying Al concertation, Al/O lateral composition was plotted from each layer as in Fig. 1 (b-f) by taking a volume of 80 nm×80 nm×2 nm in each layer as in Fig. 1(a). These Al/O ratio plots provide the visualization of local compositional variation. For layers with Al content, $x = 0.10$, 0.15 and 0.20, Al/O ratio are homogeneously distributed without any elemental variation within the layer. For the layer with $x = 0.25$, Al/O ratio varies from 0.25-0.35 which is slightly higher than those in Fig. 1(b, c and d) and can be considered as negligible. For the layer with $x = 0.30$, Al/O ratio varies from 0.2 to 0.8 showing severe elemental segregation. Initial interpretation might suggest that the segregation could result

from a poor response of the APT tip to the laser pulse due to a high bandgap with increasing Al content[27]. Additionally, in oxide materials, this kind of segregation/clustering may arise from surface diffusion of atoms due to high energy absorbed by these atoms during laser pulsing[28]. However, such segregation is not observed in $(Al_xGa_{1-x})_2O_3$ films with x = 10-20%, chemically inhomogeneous $(Al_xGa_{1-x})_2O_3$ layers are observed at $x > 0.25$. Moreover, the 1D Al/Ga concentration profile reveals no elemental diffusion within the layers (Fig. S1(b)), suggesting that the laser energy used is optimal for this material. These results also indicate $(Al_xGa_{1-x})_2O_3$ alloy at $x<0.25$ has a single chemical phase; however, at $x = 0.30$ the presence of different chemical phases is evident. Therefore, further verification is needed which we conducted in the next part of this article.

With increasing Al content, degraded crystallinity at $x = 0.30$ was observed which could be due to the presence of different chemical phases, and further increase in Al up to an extent might result in a completely different chemical phase to be dominant. Therefore, we extended our analysis over the whole compositional range with Al content, x = 0.10-1.0. Figure 2(a) demonstrates the 3D atomic map of the $(Al_xGa_{1-x})_2O_3$ heterostructure with x = 0.10, 0.20, 0.30, 0.40, 0.45, 0.50, 0.60, 0.80 and 1.0 (schematic is in Fig. S2(a)). The variation in Al content in these layers along the growth direction are visible by the contrast difference in the atomic map in Fig. 2(a). The effects of alloy composition in the layer's homogeneity are shown in Fig. 2(b-j). For layers with $x = 0.10$ and 0.20, lateral variation in Al/O ratio are homogeneously distributed without any segregation indicating these layers are single crystalline, as in Fig. 2(b, c). For the layer with x = 0.30-0.50, Al/O ratio varies over a wide range showing severe elemental segregation, suggesting, the $(Al_xGa_{1-x})_2O_3$ is no more the single crystalline structure as shown in Fig. 2(d-g). This reduced crystallinity could arise from the presence of a possible second phase within these layers. For higher Al composition, (x = 0.60-1.0) as shown in Fig. 2(h-j), lateral deviation in Al/O decreases and the layer reveals homogeneity as the Al content increases. The regaining of homogeneous Al/O distribution indicates the formation of a different single crystalline phase. Although elemental segregations are observed at layers with x = 0.30-0.50, at higher Al (x = 0.6-1.0) these segregations disappear, and instead homogeneous $(Al_xGa_{1-x})_2O_3$ layers are reformed. This implies that the Al content is not affecting the tip's response to the laser pulsing and field evaporation, which we discussed in the previous section but is directly related to the phase stability of the material.

Even though the lateral chemistry plots of the alloys indicate the presence of different chemical phases with varying Al content, PCA was applied to see if an unsupervised visualization approach would show the phase transformation trends. The typical output of APT experiments is a single TOF spectrum. Each dot in the TOF spectra represents the TOF of the collective atoms that were evaporated from the APT specimen. The TOF for atoms of any specific element is the constant, and the TOF for that element should remain the same although the TOF peak intensity varies with change in alloy chemistry. A large number of peaks are present in each TOF spectra as observed in Fig. 3(b-f) and Fig. S3(b-j). These additional peaks (given that we have only three major elements (Al, Ga and O)) are arising since the evaporated atoms of each species have different charge states such as Al^+, Al^{2+} and Al-Al^+. Therefore, each peak in the TOF spectra belongs to an element with a specific mass-to-charge state ratio and the TOF spectra with all the peaks are used as input to the PCA. Since the alloy composition, tip geometry and voltage applied are varying along the growth direction, the TOF peak for the species is also changing which is not obvious from the single TOF spectrum of the entire structure. Additionally, a benefit of our analysis is that the issues related with evaporation are captured through our analysis (by using all of the raw measurements) without our explicitly defining the effects or biasing the results. We decompose the single TOF spectrum into multiple spectra to capture the "hidden-phase" information from the APT data. This approach is illustrated in Fig. 3(a-f) for the samples with Al content, x = 0.10-0.30. A similar approach was adapted for PCA analysis for the structure with x = 0.10-1.0 and is reported in supplementary Fig. S3. The sampled TOF spectra (having TOF peaks affected by alloy composition, geometry and applied voltage) were used as the input to the analysis. In both cases, PC1 is capturing the variable most influencing the data and that is identified here as alloy composition (Al/Ga ratio along the growth direction), while PC2 represents the change in TOF peaks of the elements. This change of TOF peak is the second most influencing variable in this analysis. For $(Al_xGa_{1-x})_2O_3$ with x = 10-30%, the PCA score plots of PC1 vs. PC2 in Fig. 4(a) shows that as the Al/Ga ratio increases along the growth direction, a linearly increasing trend between alloy composition and corresponding TOF peak changes is observed up to $x \leq 0.25$. The reason for this trend is that within these layers from x = 0.10-0.25, by varying the Al content by 5% the TOF peaks do not change

much (Fig. 3(b-e)). This suggests, in these layers, a single phase is maintained although the Al content is increasing. However, for the increasing trend in PC1 vs. PC2 in Fig. 4(a), the degree of crystallinity is eventually reducing with increasing Al content. Within this Al content, x<0.25, the single crystalline $(Al_xGa_{1-x})_2O_3$ films are monoclinic β-phase stable[7-9,16]. For x>0.25, although the Al content is varied by the same 5% as the previous layers, the increasing trend between PC1 vs. PC2 is reversed (Fig. 4(a)). This trend shift is arising from a drastic change in TOF peak shape and intensity in the $(Al_xGa_{1-x})_2O_3$ layer with x = 0.30 compared to that of x = 0.25 as shown in Fig. 3(e,f). The major changes in peaks in TOF spectra from the layers with x = 0.25 to that of x = 0.30 suggests, at x = 0.30, instead of single monoclinic β-phase, multi-phase is present. A similar approach was applied to $(Al_xGa_{1-x})_2O_3$ films with x = 0.10-1.0 to capture the phase transformations over the whole composition regime as in Fig. 4(b). In the PCA analysis, from the scores plots of PC1-PC2, an increasing trend between Al/Ga ratio and TOF peak changes is observed until $x \leq 0.3$, which is an indication that even though the crystallinity is reducing as Al content is increasing, the single β-phase crystalline structure is retained up to this point. This is in agreement with the Al/O distribution results, from the lateral Al/O distribution in Fig. 2(b,c), it was observed that $(Al_xGa_{1-x})_2O_3$ film is homogeneous until x<0.30. For $x \geq 0.30$ to $x \leq 0.50$ no trend in PC1 vs. PC2 is observed (Fig. 4(b)), capturing the presence of mixed chemical phases[17] resulting in a reduced crystallinity evidenced by structural and chemical inhomogeneity in Al/O distributions in these layers as observed in Fig. 2(d-g). For Al content, $x \geq 0.60$, the downward trend in PC2 corresponds with a restoration of another crystalline phase with increasing Al content. This reformed crystalline phase could be either α or γ or η-phase stable[1],[17,18]. Formation of this single crystalline phase is correlated to the regained homogeneity of $(Al_xGa_{1-x})_2O_3$ layers with $x \geq 0.60$ as observed in lateral Al/O distribution in Fig. 2(h-j). PCA result shows phase transformation in $(Al_xGa_{1-x})_2O_3$ based on information from APT data, *i,e,* variation in TOF peaks with Al/Ga ratio. Here, we are proposing that if the primary patterns or features in the APT data can be observed independent of any interpretation (*i,e*. unsupervised learning) then we can infer the relevant information present in the data which can be easily extracted through data mining. This is an indication, if such variation in the pattern of APT data exists (for example, severe change in TOF spectrum peaks with alloy composition), it would be due to phase transformation which can be extracted via data mining. Therefore, the approach introduced here having been demonstrated can be readily applied to any further APT data measurements.

The evolution of microstructure and chemistry of MOCVD grown $(Al_xGa_{1-x})_2O_3$ with varying Al content of x = 0.10-1.0 was investigated by APT. At low Al content (x<0.25), the $(Al_xGa_{1-x})_2O_3$ films are homogeneous while layer inhomogeneity is observed at Al content of x = 0.30-0.50 due to reduced crystallinity. The film regains uniform elemental distribution with improved crystallinity at higher Al content of $x \geq 0.60$. Principal component analysis was conducted on TOF of ions to visualize the phase transformations as the alloy composition varies. The $(Al_xGa_{1-x})_2O_3$ layers are single monoclinic phase stable at Al content < 0.25 while mixed phases appear for Al composition of x = 0.30 to 0.50. $(Al_xGa_{1-x})_2O_3$ recovers the phase stability at higher Al content ($x \geq 0.60$) due to reformation of a different single crystalline phase. The data mining strategy employed on TOF of ions establishes APT as an independent characterization tool for investigating a material's structure, chemistry and chemical phases.

Supplementary materials: See supplementary materials for the schematic of the $(Al_xGa_{1-x})_2O_3$ structures with x = 0.10-0.30 and x = 0.10-1.0 used and sampling the TOF spectra of $(Al_xGa_{1-x})_2O_3$ films with x = 0.10-1.0 for PCA analysis.

Acknowledgements: Bhuiyan, Feng, Zhao acknowledge the funding support from the Air Force Office of Scientific Research FA9550-18-1-0479 (AFOSR, Dr. Ali Sayir). Feng and Zhao also acknowledge partial support from the National Science Foundation (1810041). The authors also acknowledge the contribution of Menglin Zhu (The Ohio State University) in atom probe specimen preparation.

References:

1B. W. Krueger, C. S. Dandeneau, E. M. Nelson, S. T. Dunham, F. S. Ohuchi, and M. A. Olmstead, J. Am. Ceram. Soc. 99(7), 2467 (2016).

2Y. Zhang, A. Neal, Z. Xia, C. Joishi, J. M. Johnson, Y. Zheng, S. Bajaj, M. Brenner, D. Dorsey, K. Chabak, G. Jessen, J. Hwang, S. Mou, J. P. Heremans, and S. Rajan, Appl. Phys. Lett. 112, 173502 (2018).

3D. Biswas, C. Joishi, J. Biswas, K. Thakar, S. Rajan, and S. Lodha, Appl. Phys. Lett. 114, 212106 (2019).

4E. Ahmadi, Y. Oshima, F. Wu and J. S. Speck, Semicond. Sci. Technol. 32(3), 035004 (2017).

5Q. Feng, X. Li, G. Han, L. Huang, F. Li, W. Tang, J. Zhang, And Y. Hao, Opt. Mater. Express, 7(4), 1240 (2017).

6S.-H. Yuan, C.-C. Wang, S.-Y. Huang, D.-S. Wuu, IEEE Electron Device Lett. 39 (2), 220 (2018).

7F. Zhang, K. Saito, T. Tanaka, M. Nishio, M. Arita, and Q. Guo, Appl. Phys. Lett. 105, 162107 (2014).

8Y. Zhang, T.-T. Tang, C. Girit, Z. Hao, M. C. Martin, A. Zettl, M. F. Crommie, Y. R. Shen, and F. Wang, Nature 459, 820 (2009).

9T. Oshima, T. Okuno, N. Arai, Y. Kobayashi, and S. Fujita, Jpn. J. Appl. Phys. 48(7), 070202, (2009).

10J. Li, X. Chen, T. Ma, X. Cui, F-. F. Ren, S. Gu, R. Zhang, Y. Zheng, S. P. Ringer, L. Fu, H. H. Tan, C. Jagadish, and J. Ye, Appl. Phys. Lett. 113, 041901 (2018).

11R. Miller, F. Alema and A. Osinsky, IEEE Trans. Semicond. Manuf., 31(4), 467 (2018).

12A F M A. U. Bhuiyan, Z. Feng, J. M. Johnson, Z. Chen, H-. L. Huang, J. Hwang, and H. Zhao, Appl. Phys. Lett. 115, 120602 (2019).

13V. G. Hill, R. Roy, and E. F. Osborn, J. Am. Ceram. Soc. 35, 135 (1952).

14J. Yang, P. H. Carey, S. Ahna, F. Ren, S. Jang, J. Kim, D. Hays, S. J. Pearton and A. Kuramata, ECS Trans. 80(10), 959 (2017).

15B. Mazumder, J. Sarker, Y. Zhang, J. M. Johnson, M. Zhu, S. Rajan, and J. Hwang, Appl. Phys. Lett. 115, 132105 (2019).

16S. W. Kaun, F. Wu, and J. S. Speck, J. Vac. Sci. Technol. A, 33, 041508 (2015).

17A F M A. U. Bhuiyan, Z. Feng, J. Johnson, H.-L. Huang, J. Sarker, M. Zhu, M. R. Karim, B. Mazumder, J. Hwang, and H. Zhao, APL Materials, 8, 031104 (2020).

18R. Wakabayashi, T. Oshima, M. Hattori, K. Sasaki, T. Masui, A. Kuramata, S. Yamakoshi, K. Yoshimatsu, A. Ohtomo, J. Cryst. Growth 424, 77 (2015).

19R. Miller, F. Alema and A. Osinsky, "Advances toward industrial compatible epitaxial growth of β-Ga_2O_3 and alloys for power electronics", Internation Conference on Compound Semiconductor Manufacturing Tech., (2018).

20B. Gault, M. P. Moody, F. D. Geuser, A. L. Fontaine, L. T. Stephenson, D. Haley, and S. P. Ringer, Microsc. Microanal 16, 110 (2010).

21A. Devaraj, D. E. Perea, J. Liu, L. M. Gordon, T. J. Prosa, P. Parikh, D. R. Diercks, S. Meher, R. P. Kolli, Y. S. Meng and S. Thevuthasan, Int. Mater. Rev. 63(2), 68 (2018).

22S. R. Broderick, A. Bryden, S. K. Suram, K. Rajan, Ultramicroscopy 132, 121 (2013).

23Z. Peng, Y. Lu, C. Hatzoglou, A. K. da Silva, F. Vurpillot, D. Ponge, D. Raabe and B. Gault, Microsc. Microanal. 25(2), 389 (2019).

24E.V. Mejía–Uriarte, R.Y. Sato–Berrú, M. Navarrete, O. Kolokoltsev, J. M. Saniger, J. Appl. Res. Technol. 10(10), 57 (2012).

25W. R. McKenzie, E. A. Marquis, and P. R. Munroe, Microscopy 3, 1800 (2010).

26D. J. Larson, T. Prosa, R. M. Ulfig, B. P. Geiser, and T. F. Kelly, Local electrode atom probe tomography. New York, US: Springer Science, (2013).

27L. Mancini, N. Amirifar, D. Shinde, I. Blum, M. Gilbert, A. Vella, F. Vurpillot, W. Lefebvre, R. Larde, E. Talbot, P. Pareige, X. Portier, A. Ziani, C. Davesnne, C. Durand, J. Eymery, R. Butte, J.-F. Carlin, N. Grandjean, and L. Rigutti, J. Phys. Chem. C, 118, 24136 (2014).

28D. Shinde, L. Arnoldi, A. Devaraj, and A. Vella, J. Appl. Phys. 120, 164308 (2016)

Figure caption:

Fig. 1. (a) 3D atomic map of the layered $(Al_xGa_{1-x})_2O_3$ heterostructure with varying Al composition. Only Al atoms are shown by red dots; Lateral distribution Al/O concentration ratio in each layer with Al composition of (b) $x = 0.10$, (c) $x = 0.15$, (d) $x = 0.20$, (e) $x = 0.25$ and (f) $x = 0.30$.

Fig. 2. (a) 3D atomic map of the layered $(Al_xGa_{1-x})_2O_3$ heterostructure with varying Al composition. Only Al atoms are shown by red dots; Lateral distribution Al/O concentration ratio in each layer with Al composition of (b) $x = 0.10$, (c) $x = 0.20$, (d) $x = 0.30$, (e) $x = 0.40$, (f) $x = 0.45$, (g) $x = 0.50$, (h) $x = 0.60$, (i) $x = 0.80$ and (j) $x = 1.0$.

Fig. 3. TOF sampling of the APT data for the $(Al_xGa_{1-x})_2O_3$ films with $x = 0.10$-0.30 by sectioning into equal volumes. The typical output of APT is an image of atom positions with a single TOF spectra. The first step is to divide the sample into multiple sections, each section will have a respective TOF spectrum (b) TOF spectra corresponding to each section in (a).

Fig. 4. Principal component analysis on time of flight of ions for (a) $(Al_xGa_{1-x})_2O_3$ with $x = 0.10$-0.30 and (b) $(Al_xGa_{1-x})_2O_3$ with $x = 0.10$-1.0.

Figure 1

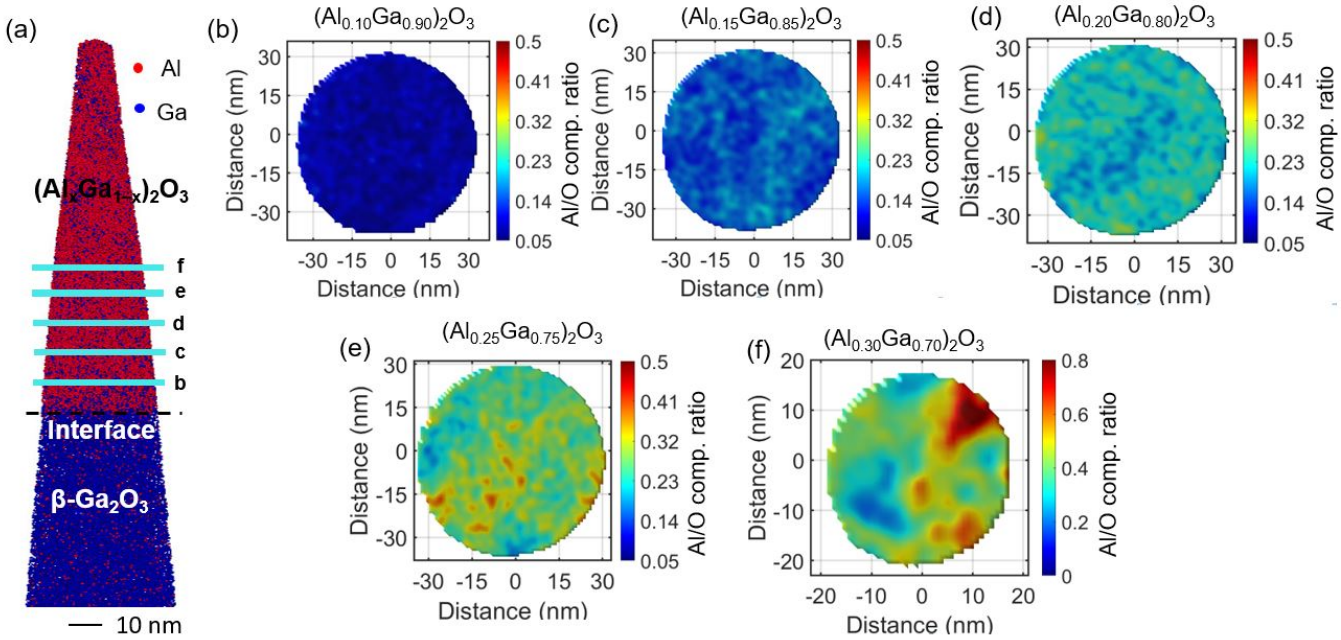
(a)
Al
Ga
$(Al_xGa_{1-x})_2O_3$
f
e
d
c
b
Interface
β-Ga_2O_3
10 nm
(b)
$(Al_{0.10}Ga_{0.90})_2O_3$
(c)
$(Al_{0.15}Ga_{0.85})_2O_3$
(d)
$(Al_{0.20}Ga_{0.80})_2O_3$
(e)
$(Al_{0.25}Ga_{0.75})_2O_3$
(f)
$(Al_{0.30}Ga_{0.70})_2O_3$
Distance (nm)
Al/O comp. ratio

Figure 2

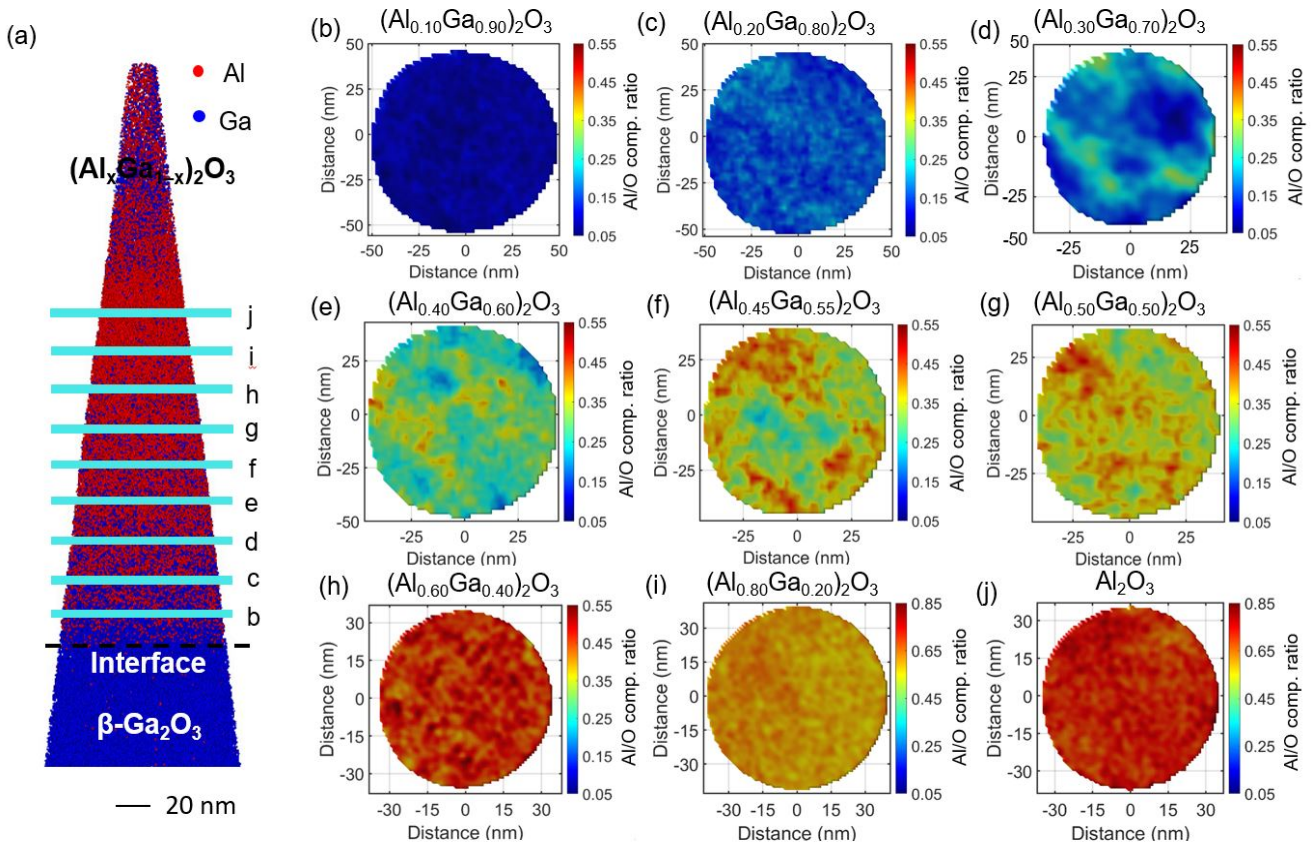
(a)
Al
Ga
$(Al_xGa_{1-x})_2O_3$
j
i
h
g
f
e
d
c
b
Interface
β-Ga_2O_3
20 nm
(b) $(Al_{0.10}Ga_{0.90})_2O_3$
(c) $(Al_{0.20}Ga_{0.80})_2O_3$
(d) $(Al_{0.30}Ga_{0.70})_2O_3$
(e) $(Al_{0.40}Ga_{0.60})_2O_3$
(f) $(Al_{0.45}Ga_{0.55})_2O_3$
(g) $(Al_{0.50}Ga_{0.50})_2O_3$
(h) $(Al_{0.60}Ga_{0.40})_2O_3$
(i) $(Al_{0.80}Ga_{0.20})_2O_3$
(j) Al_2O_3
Distance (nm)
Al/O comp. ratio

Figure 3

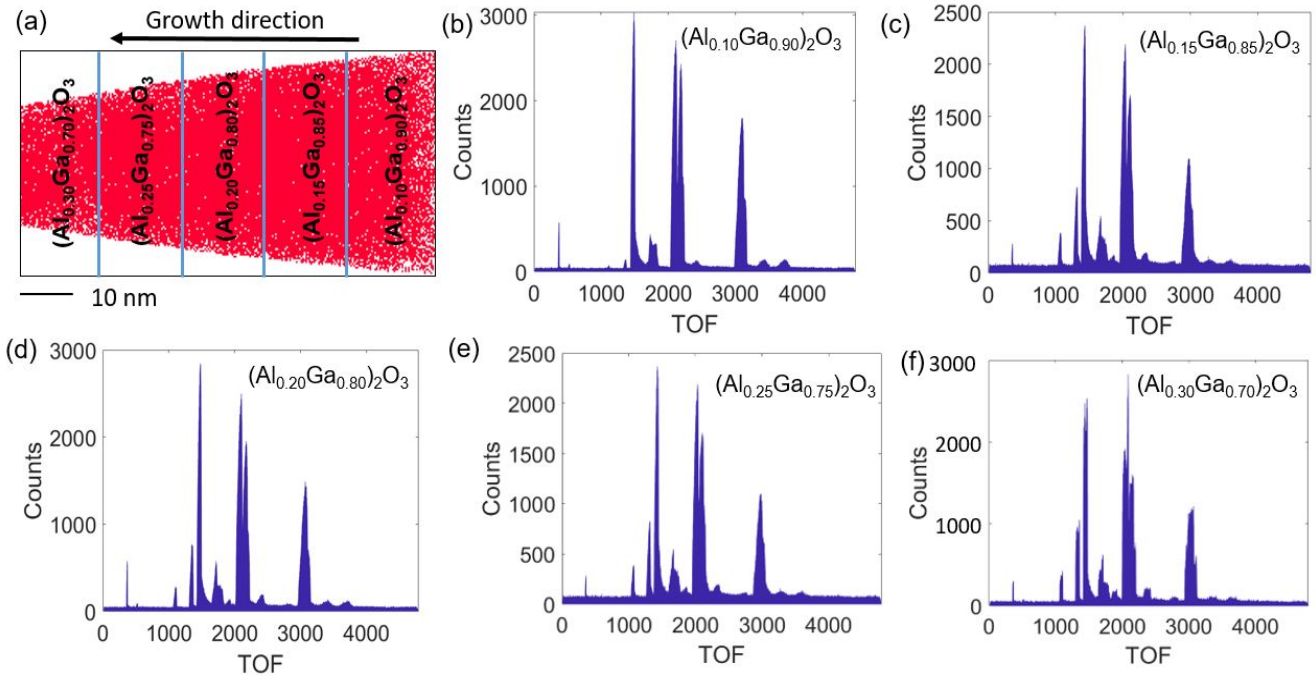
(a)
Growth direction
$(Al_{0.30}Ga_{0.70})_2O_3$
$(Al_{0.25}Ga_{0.75})_2O_3$
$(Al_{0.20}Ga_{0.80})_2O_3$
$(Al_{0.15}Ga_{0.85})_2O_3$
$(Al_{0.10}Ga_{0.90})_2O_3$
10 nm
(b)
$(Al_{0.10}Ga_{0.90})_2O_3$
Counts
TOF
(c)
$(Al_{0.15}Ga_{0.85})_2O_3$
Counts
TOF
(d)
$(Al_{0.20}Ga_{0.80})_2O_3$
Counts
TOF
(e)
$(Al_{0.25}Ga_{0.75})_2O_3$
Counts
TOF
(f)
$(Al_{0.30}Ga_{0.70})_2O_3$
Counts
TOF

Figure 4

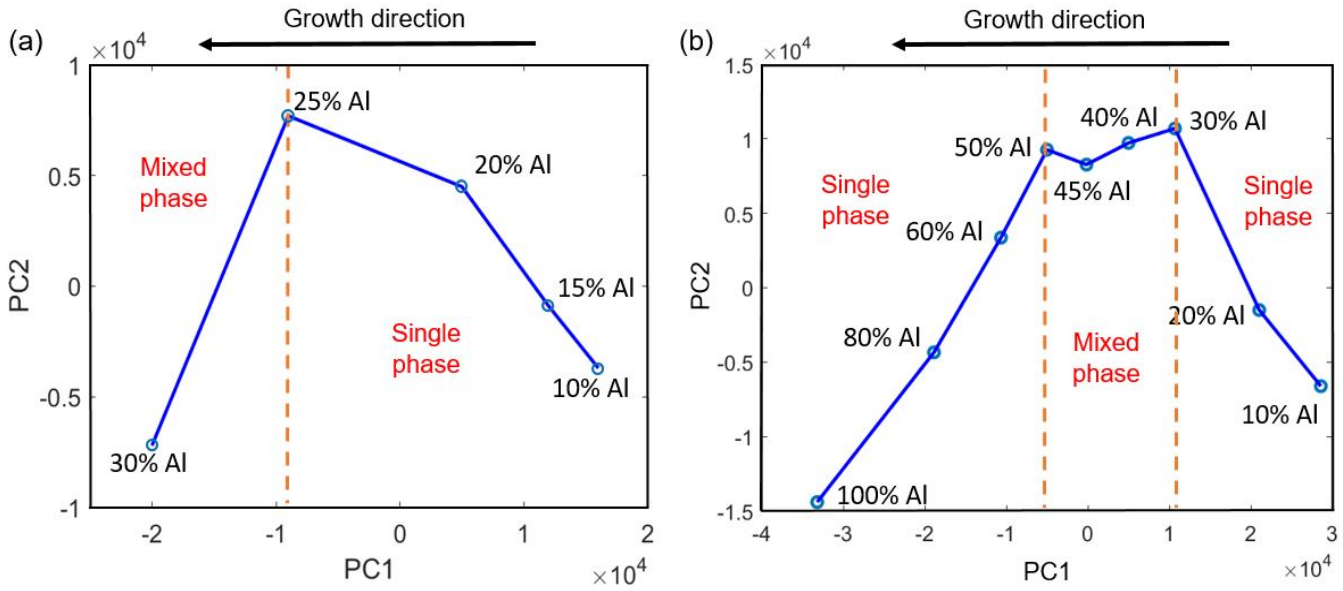
(a)
Growth direction
×10^4
1
0.5
0
-0.5
-1
PC2
-2
-1
0
1
2
PC1
×10^4
25% Al
20% Al
15% Al
10% Al
30% Al
Mixed phase
Single phase
(b)
Growth direction
×10^4
1.5
1
0.5
0
-0.5
-1
-1.5
PC2
-4
-3
-2
-1
0
1
2
3
PC1
×10^4
40% Al
30% Al
50% Al
45% Al
60% Al
80% Al
100% Al
20% Al
10% Al
Single phase
Single phase
Mixed phase